Acupuncture and Herbal Medicine

Integrated spatial metabolomics and transcriptomics reveal Ly6C$^+$ macrophage glutamine metabolism in pneumonia-mediated attenuation of aristolochic acid I nephrotoxicity

Chengxian Li[1,2], Yinkang Wang[3], Shuanglin Qin[4], Xiaoyan Zhan[3,5], Xu Zhao[3], Mingxia Fang[3], Jiaying Li[6], Ming Niu[7,*], Zhaofang Bai[3,5,*], Xiaohe Xiao[3,5,*]

[1]Institute of Traditional Chinese Medicine, Tianjin University of Traditional Chinese Medicine, Tianjin, China; [2]Haihe Laboratory of Modern Chinese Medicine, Tianjin, China; [3]Department of Liver Disease, Fifth Medical Center of Chinese PLA General Hospital, Beijing, China; [4]National Engineering Research Center of Personalized Diagnostic and Therapeutic Technology, Research Center for Precision Medication of Chinese Medicine, FuRong Laboratory, Hunan University of Chinese Medicine, Changsha, China; [5]National Key Laboratory of Kidney Diseases, Beijing, China; [6]Department of Infectious Disease, Fifth Medical Center of Chinese PLA General Hospital, Beijing, China; [7]Department of Hematology, the Fifth Medical Center of Chinese PLA General Hospital, Beijing, China

Abstract

Objective: In traditional medicine, *Asari Radix et Rhizoma* (Xi Xin) is used to effectively treat respiratory diseases. However, the therapeutic portion of Xi Xin contains trace quantities of aristolochic acid I (AAI), which raises safety concerns. Furthermore, no compelling laboratory evidence confirms its safety. AAI-induced extensive renal tubular necrosis and inflammatory cell infiltration occurred primarily in the cortex and outer medulla. Accordingly, we examined the changes in metabolites within the aforementioned areas and thoroughly investigated the interactions between these differential metabolites and immune cells.

Methods: We mapped the spatial distribution of the differential metabolites L-glutamic acid and glutamine in mouse kidneys and explored the underlying mechanisms using transcriptomics and flow cytometry, further validating these findings through co-culture experiments *in vitro*.

Results: Administering 1 mg/kg AAI daily for 7 days (approximately 200 times the pharmacopeial Xi Xin dose) did not induce detectable levels of carcinogenic 7-(deoxyadenosin-N^6-yl)-aristolactam I (dA-ALI) in mouse kidneys. However, dA-ALI was detected on the day after the administration of 10 mg/kg AAI. Mice with lipopolysaccharide-induced pneumonia exhibit increased tolerance to AAI-mediated nephrotoxicity. Based on integrated spatial metabolomics and renal transcriptomic analyses, increased tolerance to AAI-mediated nephrotoxicity may be related to glutamine-mediated oxidative stress regulation mechanisms. During pneumonia, mouse kidneys exhibit both immune and metabolic stress responses. Ly6C$^+$ macrophages convert L-glutamic acid into glutamine, thereby reducing reactive oxygen species (ROS) levels in the extracellular matrix. This process, which is regulated by the ITGA5 receptor in renal tubular epithelial cells, modulates the pAkt/pNrf2/NQO1 pathway and reduces AAI-induced kidney damage.

Conclusions: Collectively, our findings indicate that Xi Xin is safe at conventional clinical dosages, and its targeted use can further minimize potential risks.

Keywords: Aristolochic acid I, Kidney damage, Oxidative stress, Spatial metabolomics, Xi Xin safety

Introduction

A substantial proportion of plants within the Aristolochiaceae family are recognized for their medicinal properties, with Xi Xin being the most widely used[1]. For over 2,000 years, Xi Xin has been used as a principal remedy in traditional medicine for dispelling the exterior cold, warming the lungs, and transforming phlegm. In addition to its frequent inclusion in decoctions, 176 traditional Chinese patented medicines containing Xi Xin are currently used for clinical treatment. However, the presence of trace amounts of aristolochic acid I (AAI), a natural nephrotoxin, in Xi Xin markedly restricts its global application[2]. Although the 2020 edition of the Chinese Pharmacopoeia strictly regulates the AAI content in the medicinal parts of Xi Xin to less than 10 ppm, its safety remains uncertain. Currently, compelling laboratory evidence substantiating its safety is lacking.

Chengxian Li, Yinkang Wang, and Shuanglin Qin contributed equally to this work.

**Corresponding authors. Ming Niu, E-mail: nmbright@163.com; Zhaofang Bai, E-mail: baizf2008@hotmail.com; Xiaohe Xiao, E-mail: pharmacy_302@126.com.*

How to cite this article: Li CX, Wang YK, Qin SL, Zhan XY, Zhao X, Fang MX, Li JY, Niu M, Bai ZF, Xiao XH. Integrated spatial metabolomics and transcriptomics reveal Ly6C$^+$ macrophage glutamine metabolism in pneumonia-mediated attenuation of aristolochic acid I nephrotoxicity. Acupunct Herb Med 2025;5(3):301–315. doi: 10.1097/HM9.0000000000000165

Received 27 February 2025 / Accepted 07 July 2025

Traditional safety studies on Xi Xin have primarily focused on the chemistry and toxicology of its toxic component, aristolochic acid, and have overlooked the clinical context of its application. Typically, drugs are used by patients with morbid conditions, and drug metabolism can differ substantially between physiological and pathological states[3]. Therefore, in drug safety research, careful attention should be paid to animal models of morbidity[4]. Considering the frequent clinical use of Xi Xin in the treatment of respiratory diseases, we established a pneumonia model using 2 mg/kg lipopolysaccharide (LPS). In this study, we integrated spatial metabolomics and transcriptomics to determine the differences in the responses and mechanisms of AAI-induced kidney damage between mice with pneumonia and normal mice.

The AAI-induced nephrotoxic effects include nephrotoxicity and carcinogenicity. Nephrotoxicity primarily manifests as damage to renal tubules, whereas carcinogenicity is based on DNA adduct formation. AAI undergoes bioactivation in the kidneys and other organs, forming reactive intermediates that covalently bind to DNA bases. The most representative and stable DNA adduct that results from this process is 7-(deoxyadenosin-N6-yl)-aristolactam I (dA-ALI). This adduct predominantly forms at adenine residues in DNA, and is considered a critical molecular event underlying AAI-induced mutagenesis and carcinogenesis. DA-ALI exhibits high stability *in vivo* and is resistant to repair, leading to characteristic A:T → T:A transversion mutations. These mutations serve as the molecular "fingerprints" of AAI exposure. Thus, the relationship between AAI and dA-ALI not only elucidates the chemical carcinogenic mechanism of aristolochic acid but also provides a crucial basis for environmental exposure assessment and molecular epidemiological studies. In this study, we established an external standard detection method for dA-ALI and conducted methodological testing to ensure precise measurement of DNA adduct content. Spatial metabolomics, a technique for studying the spatial distribution of metabolites within tissues or organs, offers unique advantages for examining changes in renal metabolite distribution during pneumonia[5–6]. The use of high-resolution airflow-assisted desorption electrospray ionization mass spectrometry (MS) imaging, an *in situ* spatial metabolomics approach, has revealed that AAI-induced extensive renal tubular necrosis and inflammatory cell infiltration primarily occurs in the cortex and outer medulla[7]. Therefore, in the present study, we used spatial metabolomics to examine changes in metabolites within the aforementioned areas and thoroughly investigated interactions between these differential metabolites and immune cells.

Materials and methods

Chemicals and reagents

AAI was purchased from MCE (Shanghai, China) and dA-ALI (CAS: 127191-86-0) was synthesized by WuXi AppTec (Shanghai, China). The StarRuler Color Prestained Protein Marker (Cat. No. M221), 10× Tris-Glycine Electrophoresis Buffer (Cat. No. E152-01), and 10 × Wet Transfer Buffer (Cat. No. E173-01) used in the Western blot experiments were all purchased from GenStar (Beijing, China). The sources of other experimental reagents and consumables are provided in the Supplementary Materials (Supporting Reagents, https://links.lww.com/AHM/A182).

Animals

C57BL/6J male mice [8-week-old, (20 ± 2) g; specific pathogen-free grade, Experimental animal certificate number No. 110324220105758876] were purchased from SPF Biotechnology Co., Ltd. (Beijing, China). Mice were maintained under pathogen-free conditions. All mice were provided unlimited water and food and were maintained under a 12-hour dark/light cycle (25 ± 2)°C. All animal experiments were performed in accordance with the Guidelines for the Care and Use of Laboratory Animals and were approved by the Fifth Medical Centre of the PLA General Hospital, Beijing, China (ethical approval No. IACUC-2021-0010). Mice were anesthetized using 2% isoflurane (Yuyan Anesthetic Breathing System, Shanghai, China).

Relationship between the dose of AAI administered and the level of DNA adducts

Seventy-two mice were randomized into four groups using a random number table method (Figure 1A). AAI was administered *via* oral gavage at doses of 0.01, 0.1, 1, and 10 mg/kg. Tissue samples were collected on days 1, 4, and 7 (n = 6 per time point) *via* rapid euthanasia, followed by kidney harvesting for dA-ALI testing.

Mouse models with pneumonia and without pneumonia

Using a random number table method, 24 mice were equally divided into four groups (n = 6 each). A pneumonia model was established by tracheal instillation of LPS before intratracheal instillation, after which the mice were fully anesthetized with 2% isoflurane and secured in a suspended position on a triangular bracket. A spotlight was used to illuminate the neck region, and the tongue was gently pulled laterally using forceps to expose the trachea within the visual field. A 22G intravenous catheter (0.9 mm in diameter, 25 mm in length, with the plastic tubing extending 2 mm beyond the needle tip) was inserted through the oral cavity to perform tracheal intubation. Subsequently, 50 μL of LPS (2 mg/mL) was slowly instilled through the catheter. After instillation, the mice were maintained in a head-up and feet-down position for approximately 1 to 2 min while the triangular bracket was gently rotated to ensure uniform distribution of the liquid throughout the lung. Groups receiving a single treatment were designated as single inflammation (SI) groups, and their corresponding controls were deemed single controls (SC). Groups receiving multiple treatments were named enduring inflammation (EI), while their control was referred to as enduring control (EC). Twelve hours after LPS administration, AAI (10 mg/kg) was administered *via* oral gavage. At designated time

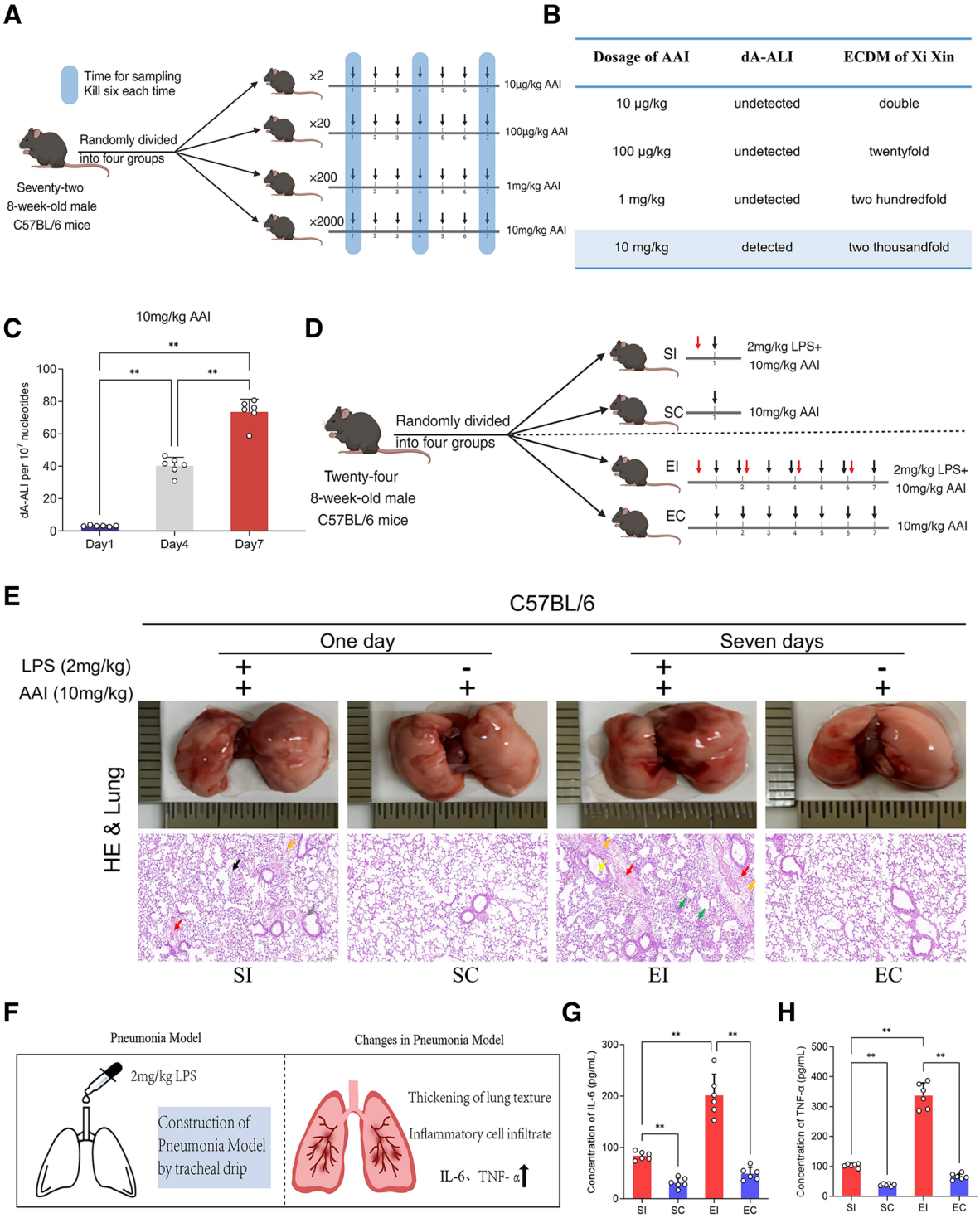

Figure 1. Dose-time carcinogenic toxicity of AAI and construction and validation of a pneumonia model. (A) Grouping of dose-time-toxicity experiments. (B) Dose-time carcinogenic toxicity of AAI. (C) Formation of dA-ALI in the kidneys of mice administered 10 mg/kg AAI. (D) Grouping of morbid animal experiments. (E) Morphological images and H&E staining results of mouse lungs (black arrows indicate minimal macrophage infiltration, yellow arrows show minimal lymphocyte infiltration, red arrows indicate minimal hemorrhage, and green arrows represent interstitial edema). (F) Construction of the pneumonia model. (G and H) Expression levels of inflammatory markers in bronchoalveolar lavage fluid ($n = 6$; $^{**}P < 0.01$). AAI: Aristolochic acid I; dA-ALI: 7-(Deoxyadenosin-N^6-yl)-aristolactam I; EC: Enduring control; ECDM: Equivalent clinical dose method; EI: Enduring inflammation; H&E: Hematoxylin and eosin; IL-6: Interleukin-6; LPS: Lipopolysaccharide; SC: Single control; SI: Single inflammation; TNF-α: Tumor necrosis factor-α.

points, the mice were anesthetized and bronchoalveolar lavage fluid was collected, followed by cardiac puncture for blood sampling. Subsequently, the lungs and kidneys were harvested. One kidney was immediately snap-frozen in liquid nitrogen for multiomics analysis. The other kidney was bisected along the coronal plane; one half was used for flow cytometry, and the other half was immersed in 10% formalin along with the lungs.

Biochemical analysis and histopathological staining

To obtain serum, the blood was centrifuged twice at 3,500 rpm for 15 min. Then, serum levels of blood urea nitrogen (BUN), creatinine (Cr), interleukin (IL)-6, tumor necrosis factor (TNF)-α, and oxidative stress markers were measured in accordance with the instructions of the respective assay kits. Paraffin-embedded and frozen sections were stained with hematoxylin and eosin (H&E) to identify histopathological changes. The γ-H2AX protein in the sample was immunohistochemically stained using an antibody dilution ratio of 1:9,000 (cat: ab11174; Abcam, USA).

Analysis of dA-ALI

DA-ALI was synthesized by WuXi AppTec, as reported by Wang et al.[8–9], with an average purity of 98.35% as determined using high-performance liquid chromatography (HPLC). Details of the ^{1}H NMR spectra, MS, and additional HPLC results are provided in the Supplementary Materials (Identification of dA-ALI standard samples, https://links.lww.com/AHM/A182). Using standard dA-ALI, we established a liquid chromatography-MS (LC-MS) method to measure adduct content in animal bodies. The specific methods are detailed in the Supplementary Materials (Supporting Methods 1, https://links.lww.com/AHM/A182). The method for digesting animal tissue DNA is described in our previously published study[10].

Transcriptomics and bioinformatics analysis

RNA transcriptome sequencing was performed using three mouse kidney samples from the SI, SC, EI, and EC groups. The experimental workflow included the following steps.

Total RNA was extracted using the MagZol reagent. RNA integrity and purity were assessed using agarose gel electrophoresis, NanoPhotometer (Qubit, Agilent 2100).

The RNA libraries were constructed using the NEBNext Ultra RNA Library Prep Kit. The mRNA was first enriched using oligo(dT) magnetic beads, followed by fragmentation and reverse transcription to synthesize double-stranded cDNA. After end repair, A-tailing, adaptor ligation, PCR amplification, and purification, libraries were constructed.

Libraries were quantified using Qubit, assessed for insert size using Agilent Technologies, and quantified using qPCR. Qualified libraries were then subjected to 150 bp paired-end sequencing on the Illumina platform.

Sequencing data were filtered using fastp, aligned to the mouse reference genome (GRCm39.109) using HISAT2, and gene expression levels (FPKM) were calculated. Differentially expressed genes were identified using DESeq2 ($|\log2FC| \geq 1$, FDR < 0.05), followed by Gene Ontology (GO) and Kyoto Encyclopedia of Genes and Genomes (KEGG) enrichment analyses.

Matrix-assisted laser desorption ionization time-of-flight (MALDI-TOF) MS for spatial metabolomics

Sample preparation and MALDI-TOF measurement

Briefly, the frozen kidney tissue samples were embedded in gelatin and fixed in three drops of distilled water. The tissues were sectioned at 10-μm thickness using a Leica CM1950 cryostat (Leica Microsystems GmbH, Wetzlar, Germany) at –20°C. Subsequently, the tissue sections were placed in groups on electrically conductive slides coated with indium tin oxide (ITO), and the slides with tissue sections were dried in a vacuum desiccator for 30 min. A solution of 2,5-dihydroxybenzoic acid was prepared using 90% acetonitrile and 10% water. The 2,5-dihydroxybenzoic acid matrix solution was uniformly sprayed onto ITO slides containing tissue sections using a TM-Sprayer (Bruker Daltonics, Bremen, Germany). The ITO slides coated with the matrix were placed on a mass spectrometer target plate, and tissue areas were selected using the DataImaging software (Bruker, Billerica, MA, USA) for MALDI-TOF measurements.

MALDI timsTOF mass spectrometric imaging experiments were performed using a prototype Bruker timsTOF flex MS system (Bruker Daltonics) equipped with a 10 kHz smartbeam 3D laser. The laser power was fixed at 80% throughout the experiments. Mass spectra were acquired in the positive mode. Mass spectral data were acquired over a mass range of mass-to-charge ratio (*m/z*) 50 to 1,300 Da. The imaging spatial resolution was set to 50 μm for the tissue, and each spectrum consisted of 400 laser shots.

Data processing and analysis

Under laser excitation, the tissue samples were ionized with the matrix, and the released molecules were identified using a mass spectrometer. This process generated raw data on the *m/z* and peak intensity for each pixel of the sample. The raw data were imported into the SCiLS Lab software for smoothing and root mean square normalization. This generates information on the relative intensities of different *m/z* values at each spatial point, which are then translated into pixels on the imaging heatmaps[11]. By aligning H&E-stained images of adjacent sections, precise extraction of MS profiles from regions of interest can be achieved, generating individual two-dimensional data matrices (*m/z*, intensity)[7,12]. MS/MS fragmentations performed on the timsTOF flex MS system in MS/MS mode were used for further detailed structural confirmation of identified metabolites.

Western blotting

Proteins were extracted from the cell lysate (2 mL) and liver tissue (30 mg) as previously described[10]. Subsequently, the samples were heated at 105°C for 15 min and subjected to 10% sodium dodecyl sulfate-polyacrylamide gel electrophoresis. The proteins were then transferred onto nitrocellulose membranes using a wet-transfer system. The rapid sequestration chamber was sealed for 10 min and incubated overnight with the target protein. The following day, the specimens were incubated with a secondary antibody for 1 h to develop the images. Signals were analyzed using enhanced chemiluminescence reagents (Promega, Beijing, China).

Flow cytometry for quantification of Ly6C$^+$ macrophages

Fifty milligrams of kidney tissue were minced and transferred to a clean glass slide, where they were minced

into a paste. The obtained paste was then placed in 2 mL of Dulbecco's modified Eagle Medium containing 10% fetal bovine serum (FBS), 0.5 mg/mL collagenase IV, and 0.05 mg/mL DNase I, and incubated at 37°C for 60 min until complete tissue digestion was achieved. The digest was sequentially strained through 200- and 400-mesh sieves and collected in a 15 mL centrifuge tube. The mixture was centrifuged at 1,200 rpm for 8 min and the supernatant was discarded. The pellet was resuspended in 4 mL of 1× phosphate-buffered saline (PBS), centrifuged again at 1,200 rpm for 8 min, and the cells were resuspended in PBS. Cell suspension was adjusted to 1×10^7 cells/mL, and 100 µL of the single-cell suspension was aliquoted per tube for labeling. Subsequently, the cells were processed by Fc receptor blocking, surface antibody staining, red blood cell lysis, and washing before being resuspended for flow cytometry.

In vitro Ly6C$^{\pm}$ macrophage co-cultures with mouse renal tubular epithelial cells (mRTECs)

After centrifugation, as described in the Western blotting section, to obtain cell pellets, the cells were resuspended in PBS containing 2% FBS to establish a single-cell suspension for flow cytometric sorting. The sorted cells, specifically the CD45$^+$CD11b$^+$F4/80$^+$Ly6C$^+$ and CD45$^+$CD11b$^+$F4/80$^+$Ly6C$^-$ populations, were collected into 15 mL centrifuge tubes containing RPMI 1640 medium (Cat No.: 21870092; Gibco, Waltham, MA, USA) supplemented with 20% FBS and prepared for subsequent co-culture experiments. A total of 300,000 Ly6C$^+$ or Ly6C$^-$ cells were seeded in the upper chambers of a 24-well transwell plate with a 0.1-µm polycarbonate membrane. Concurrently, 100,000 mRTECs were seeded in the lower wells of the RPMI 1640 medium supplemented with glutamine (Cat No.: 11875093; Gibco). After 8 h, the medium was discarded after the cells adhered, and the cells were washed once with PBS. RPMI 1640 medium without Glutamine (700 µL in the lower chamber and 100 µL in the upper chamber) was added. Subsequently, 10 mM L-glutamic acid was added to the upper chamber, with 100 µM AAI added to the lower chamber. Following incubation at 37°C for 24 h, supernatants from the lower chamber and mRTECs were collected for subsequent analysis.

LC-MS for L-glutamic acid and glutamine

Supernatant samples from each group were diluted tenfold with sterile enzyme-free water and analyzed using LC-MS (SCIEX QTRAP 6500 plus, USA). L-Glutamic acid and glutamine were monitored in multiple reaction monitoring (MRM) mode with transitions at *m/z* 148.2/84.1 (CE: 20) and *m/z* 147.2/130.0 (CE: 13), respectively. The peak areas were recorded, integrated into the calibration curve, and multiplied by the dilution factor to determine the precise analyte concentrations. Detailed LC-MS methods and results are provided in the Supplementary Materials (Supporting Methods 2, https://links.lww.com/AHM/A182).

DCFH-DA for changes in ROS in mRTECs

Briefly, mRTECs were fixed with 4% paraformaldehyde for 1 min to preserve the cell morphology. After washing twice with PBS, 100 µL of DCFH-DA solution (diluted to 10 µM in serum-free RPMI 1640 medium) was added to each well and incubated at 37°C for 30 min. Unbound fluorescent probes were washed off with PBS, followed by the addition of 100 µL Hoechst solution (10 µg/mL) to each well. After incubating for 5 min at 37°C and a subsequent PBS wash to remove unbound Hoechst, fluorescence intensity was measured using a fluorometer (BioTek; Synergy H1, USA); the cells were observed under a light microscope (Leica, Wetzlar, Germany).

Results

Dose-time carcinogenic toxicity of AAI and dA-ALI generation

To investigate the dose-time carcinogenic toxicity of AAI, mice were divided into various dose groups, and tissue samples were collected on days 1, 4, and 7 after AAI administration (Figure 1A). After the administration of 0.01, 0.1, and 1 mg/kg AAI for 7 d, dA-ALI remained undetectable in the kidneys of the mice (Figure 1B).

However, at a dose of 10 mg/kg, dA-ALI was detected in the kidneys 1 day after administration, and its concentration increased with the duration of gavage ($n = 6$, $P < 0.01$). The dA-ALI concentration in mouse kidneys from days 1 to 7 ranged from 2.7 to 80.7 adducts per 10^7 nucleotides (Figure 1C).

LPS-induced pneumonia model exhibits pronounced inflammatory responses

A pneumonia model was established by the tracheal instillation of 2 mg/kg LPS into each mouse in the experimental group (Figure 1F). Compared with the control, SC, and EC groups, the SI and EI groups exhibited macroscopically visible changes (Figure 1D), including varying degrees of congestion, edema, and scar formation on the lung surface, with more pronounced changes observed in the EI group. H&E staining revealed different levels of inflammatory cell infiltration, with a more pronounced infiltration observed in the EI group (Figure 1E). In addition, we measured levels of IL-6 and TNF-α, representative markers of the LPS-induced pneumonia model[13–14]. Treatment with 2 mg/mL LPS significantly increased the levels of both IL-6 ($P < 0.01$; Figure 1G) and TNF-α ($P < 0.01$; Figure 1H) in the bronchoalveolar lavage fluid of mice.

Single-dose administration reduces AAI-induced renal damage by inhibiting the expression of NQO1

H&E staining of kidney tissues collected after the first and seventh administrations demonstrated a progressive increase in pathological renal damage. Compared to single dosing, repeated administration resulted in more severe histopathological alterations, indicating cumulative renal toxicity. Further intragroup analysis revealed the order of severity as follows: SI < SC < EC < EI

(Figure 2A; $n = 3$). The renal function indicators, serum Cr (Figure 2B; $n = 6$) and BUN (Figure 2C; $n = 6$), were significantly lower in the SI group than in the SC group ($P < 0.05$). However, after 7 days of pneumonia, no significant differences were observed in the serum Cr and BUN levels between the EI and EC groups. In addition, leveraging the characteristic AAI-induced DNA damage, we used γ-H2AX antibody staining to stain nuclei with DNA double-strand breaks (Figure 2D)[15–16]. According to the immunohistochemistry results, the proportion of positive nuclei followed the pattern of SI < SC < EI < EC (Figure 2E; $n = 3 \times 3$, $P < 0.01$). To assess the differences in the carcinogenic response to AAI between mice with pneumonia and normal mice more accurately, we measured dA-ALI levels in the kidneys of each group. The levels of the DNA adduct dA-ALI showed a trend of SI < SC < EI ≈ EC ($n = 6$, $P < 0.01$; Figure 2F). Collectively, these findings suggested that single-dose administration reduced renal damage; however, this effect was not observed in the multiple-dose groups.

Considering that AAI-induced renal toxicity and carcinogenicity are mitigated to varying extents under short-term pneumonia conditions, we hypothesized that the levels of the enzymes involved in AAI metabolism may be altered. Therefore, we performed western blot analysis to measure the levels of AAI-related metabolic enzymes CYP1A1/2 and NQO1 in the kidneys (Figure 3A). Densitometric analysis revealed that the levels of CYP1A1/2 were similar across all groups. Conversely, NQO1 levels in the SI group were lower than in the SC group ($P < 0.01$; Figure 3B) and higher in the EI group than in the EC group ($P < 0.01$; Figure 3B).

Transcriptomic analysis reveals the potential mechanisms through which pneumonia status affects renal NQO1 protein expression

Short-term pneumonia enhances the antioxidative stress capacity of the kidneys

Based on RNA-sequencing data collected from the SI, SC, EI, and EC groups (see Transcriptomics and bioinformatics analysis section and Supplementary Materials, https://links.lww.com/AHM/A182), principal component analysis (Figure 3C and D) and cluster heatmap (Figure 3E and F) revealed distinct differences between the LPS-treated and control groups with good intragroup sample similarity. The top 10 differentially expressed genes are presented in the form of a volcano plot [Supplementary Figure S1A and B, https://links.lww.com/AHM/A182]. Subsequently, enrichment analysis was performed using GO. Based on the multi-group GO enrichment bar chart (Figure 3G), the SI_VS_SC group had more obvious enrichment in detoxification and antioxidant activity than the EI_VS_EC group, suggesting that the reduction in AAI-induced renal damage during short-term pneumonia could be attributed to the modulation of the antioxidant activity of the body. Furthermore, gene set enrichment analysis of oxidative stress-related pathways from the KEGG data revealed the top 10 ranked pathways (Figure 3H).

ROS-mediated ITGA5/pAkt/phosphorylated Nrf2 (pNrf2) pathway is involved in regulating NQO1 expression in mice kidneys

To validate our hypothesis, oxidative stress markers were analyzed in serum (Figure 4A1–4) and tissues (Figure 4B1–4). The SI group exhibited higher levels of superoxide dismutase, glutathione (GSH), and total GSH/GSH disulfide in the kidneys than in the SC group; the opposite was observed in the serum. These findings indicate that the kidneys of the SI group possessed greater antioxidative stress capacity and lower levels of oxidative stress than those of the SC group. Accordingly, short-term pneumonia can induce increased serum oxidative stress levels, subsequently activating the renal antioxidative defense mechanisms. However, this effect disappeared after persistent pneumonia for 7 days, as evidenced by the serum and renal oxidative stress markers showing a trend of EI < EC.

We hypothesized that the phosphoinositide 3-kinase (PI3K-Akt) signaling pathway is involved in regulating Nrf2 phosphorylation, subsequently affecting the expression of NQO1. Transcriptomic results indicated that the upstream ITGA proteins in the PI3K/AKT pathway were downregulated [Supplementary Figure S2A, https://links.lww.com/AHM/A182] in the SI_VS_SC group and were upregulated [Supplementary Figure S2B, https://links.lww.com/AHM/A182] in the EI_VS_EC group (Figure 4C). Therefore, we investigated the most variably expressed ITGA subtypes, ITGA5 and ITGA8 by using The Human Protein Atlas database. ITGA5 is expressed on the membranes of renal tubular epithelial cells, whereas ITGA8 is localized to the membranes of glomerular cells. Given that AAI toxicity primarily targets renal tubular epithelial cells[17–18], we postulated that ITGA5 could detect changes in environmental ROS levels, leading to alterations in the expression of downstream pathway proteins. This hypothesis was supported by the results of western blot analysis (Figure 4H), which showed that low levels of ROS in the SI group corresponded to relatively low expression of the ITGA5/pAkt/pNrf2 pathway. This suppression in turn suppressed NQO1 expression and enhanced renal tolerance to AAI-induced damage in mice.

Flow cytometry analysis shows that renal Ly6C⁺ macrophages participate in the spontaneous antioxidative stress response in the body

Kidney transcriptome KEGG enrichment scatter plots revealed significant changes in antigen processing and presentation pathways in both SI_VS_SC (Figure 5A) and EI_VS_EC (Figure 5B) groups. The cells closely associated with this function include dendritic cells, macrophages, and B cells, which are key antigen-presenting cells. To identify the cell type exhibiting the most significant changes in abundance, we analyzed immune cell infiltration in mouse kidney transcriptomic data, as described by Chen et al.[19] Heatmap results (Figure 5C and D) indicated noticeable changes in the macrophage population. Flow cytometric analysis was performed to quantify renal Ly6C⁺ macrophages using the gating strategy detailed in Figure 5E1–5. The SI group showed a significant increase

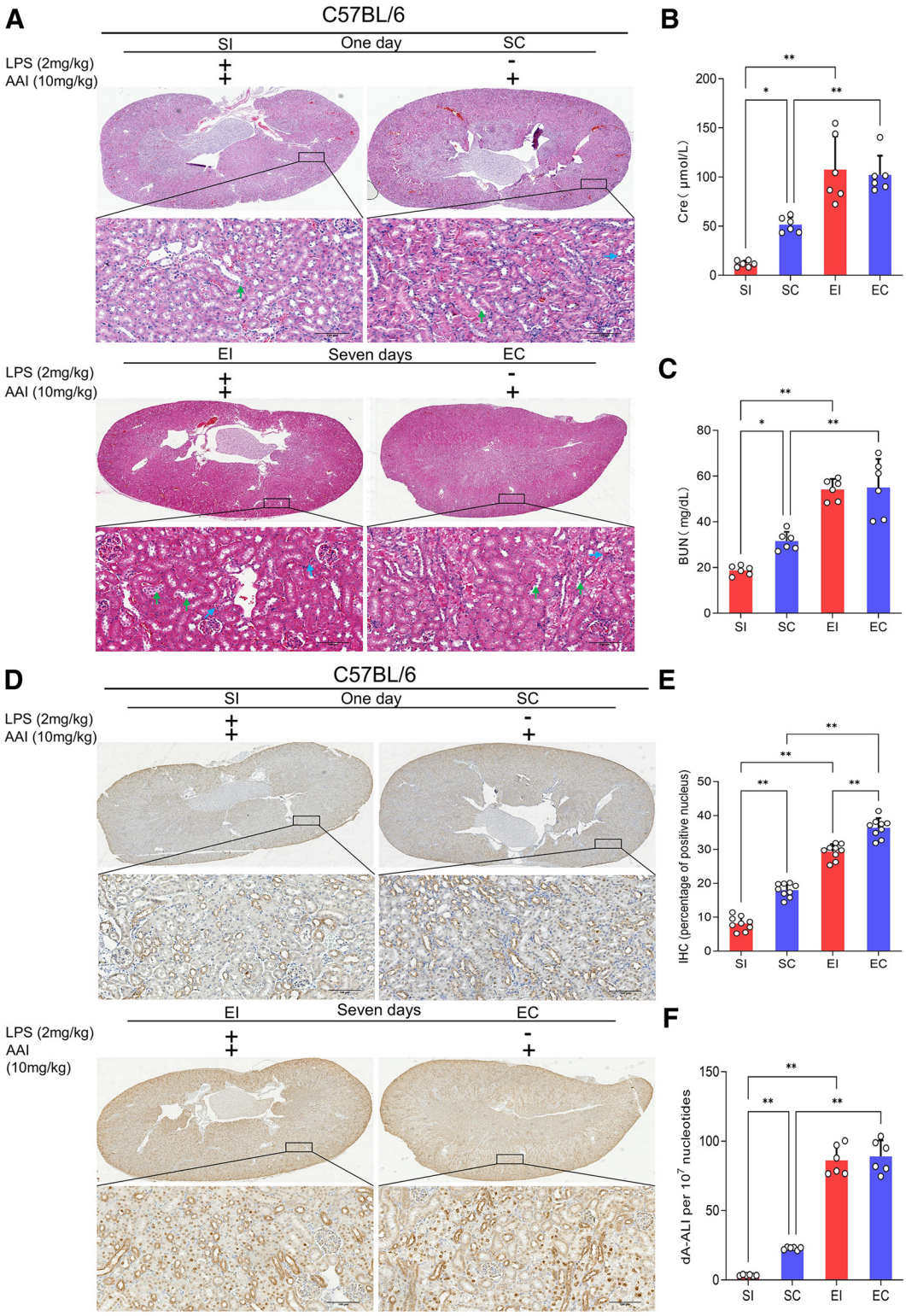

Figure 2. Differential cytotoxic and carcinogenic effects of AAI on C57BL/6 mouse kidneys. (A) Representative images of H&E-stained sections of the kidneys ($n = 3$, scale bars: 100 μm; blue arrows indicate tubular epithelial cell shedding and green arrows show the degree of inflammatory cell infiltration). (B and C) Renal functional indicators, and serum creatinine and blood urea nitrogen levels ($n = 6$). (D) IHC for γ-H2AX protein ($n = 3$, scale bars: 100 μm). (E) Quantification of IHC-positive nuclei ($n = 3 \times 3$). (F) Differences in renal dA-AAI content. (*$P < 0.05$, **$P < 0.01$). AAI: Aristolochic acid I; dA-ALI: 7-(Deoxyadenosin-N^6-yl)-aristolactam I; EC: Enduring control; EI: Enduring inflammation; H&E: Hematoxylin and eosin; IHC: Immunohistochemistry; LPS: Lipopolysaccharide; SC: Single control; SI: Single inflammation.

in Ly6C$^+$ macrophages compared to the SC group ($P < 0.01$; Figure 5F), whereas no significant differences were detected between the EI and EC groups, suggesting that Ly6C$^+$ macrophages may be involved in the spontaneous antioxidative stress response of the body.

Spatial metabolomics reveals that oxidative stress levels impact renal L-glutamic acid levels

The kidney is divided into distinct regions based on its tissue structure: the cortex, outer medulla (outer

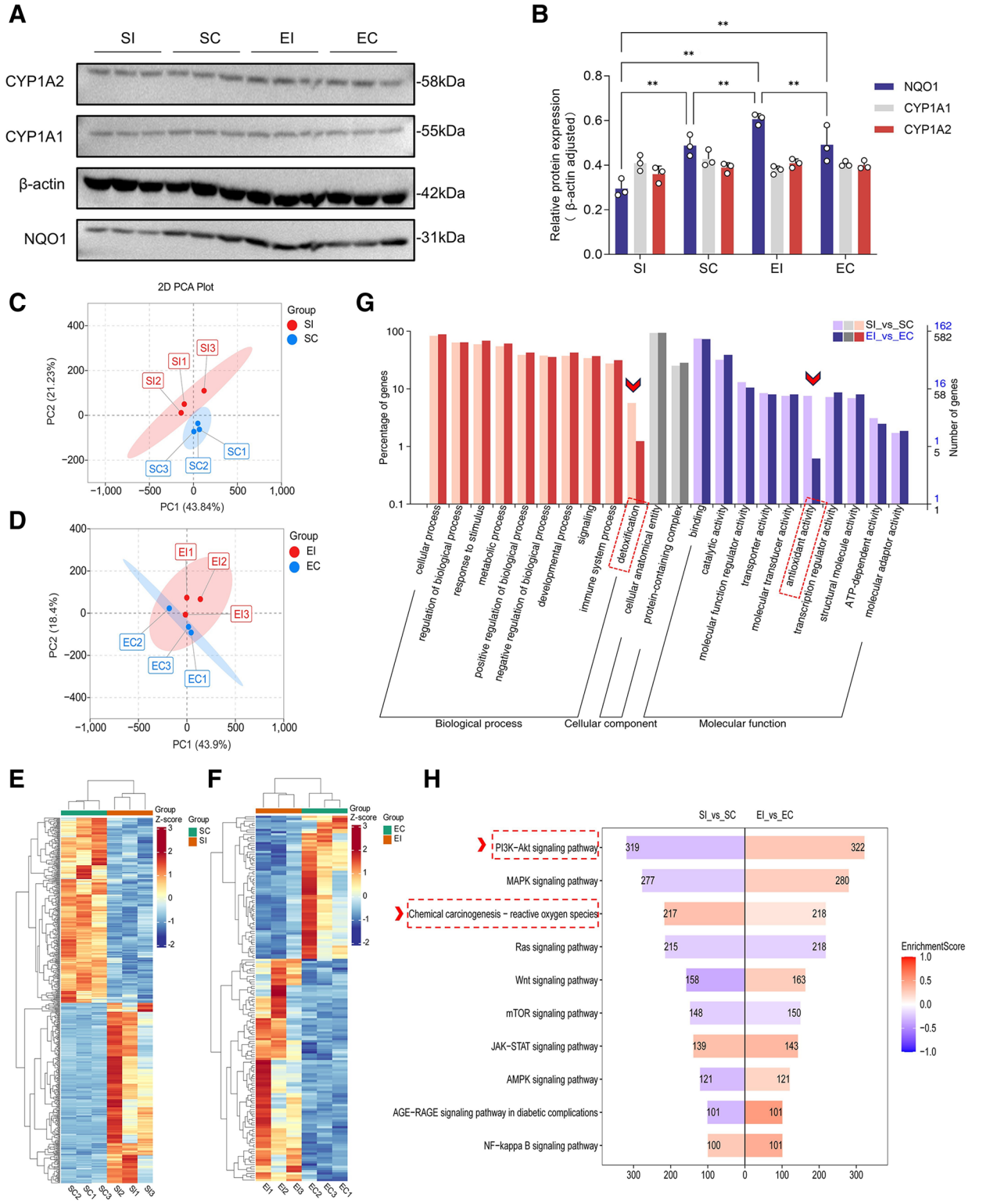

Figure 3. Transcriptomic study of differences in AAI-induced kidney damage in C57BL/6 mice. (A and B) Western blot analysis of the primary metabolic enzymes for AAI and corresponding densitometric analysis (**$P < 0.01$). (C and D) Principal component analysis results for the single- and multiple-dose groups. (E) Cluster heatmap for the SI_VS_SC group. (F) Cluster heatmap for the EI_VS_EC group. (G) Multi-group Gene Ontology functional enrichment analysis bar chart. (H) Gene set enrichment analysis butterfly plot. AAI: Aristolochic acid I; EC: Enduring control; EI: Enduring inflammation; IHC: Immunohistochemistry; PI3K-Akt: Phosphoinositide 3-kinase; SC: Single control; SI: Single inflammation.

and inner stripes), and inner medulla (Figure 6A)[20]. Damage inflicted by aristolochic acid on mouse kidneys predominantly occurs across the cortex and corticomedullary junction (outer stripe)[7]. In this study, the kidneys were spatially divided into three areas: A, B, and C, corresponding to the cortex, outer stripe, and the rest, respectively. The SI_VS_SC and EI_VS_EC groups were analyzed according to these three regions, and the results are depicted in a petal Venn diagram (Figure 6B), which identified L-glutamic acid (m/z = 148.0604) as the only shared differential metabolite. We further analyzed regions A and B, and

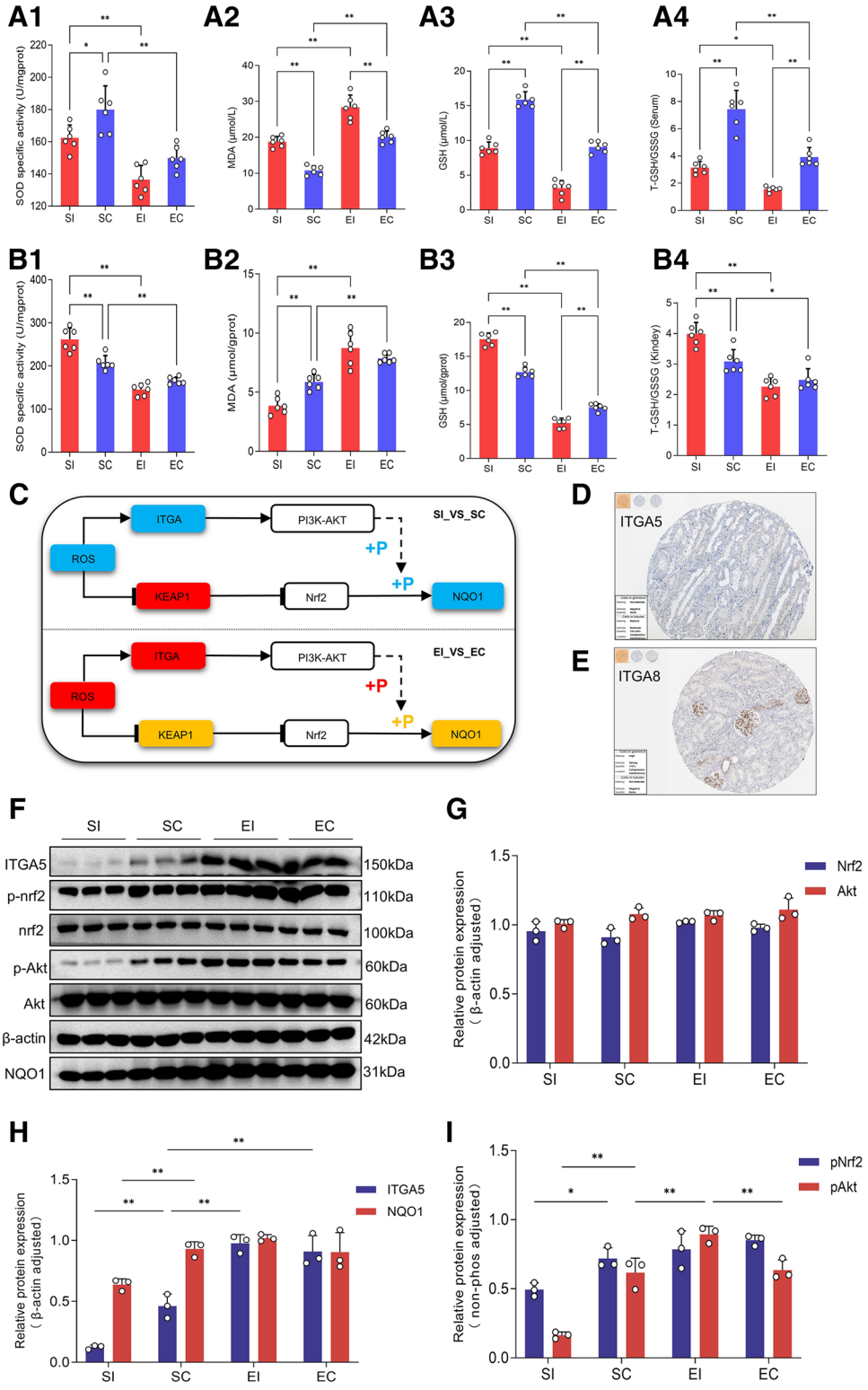

Figure 4. ROS-mediated regulation of NQO1 expression through the ITGA5/pAkt/p-Nrf2 pathway. (A1–A4) Oxidative stress markers in mouse serum: SOD, MDA, GSH, and T-GSH/GSSG. (B1–B4) Oxidative stress markers in mouse kidney tissue: SOD, MDA, GSH, and T-GSH/GSSG. (C) Schematic illustrating the potential pathway for ROS-regulated NQO1 expression (blue indicates low levels, orange indicates moderate levels, and red indicates high levels). (D and E) IHC of ITGA5 and ITGA8 in renal tissue from The Human Protein Atlas database. (F–I) Western blot results and densitometric analysis of the ITGA5/pAkt/p-Nrf2 pathway. (*$P < 0.05$, **$P < 0.01$). EC: Enduring control; EI: Enduring inflammation; GSH: Glutathione; GSSG: GSH disulfide; MDA: Malondialdehyde; PI3K-Akt: Phosphoinositide 3-kinase; ROS: Reactive oxygen species; SC: Single control; SI: Single inflammation; SOD: Superoxide dismutase; T-GSH: Total GSH.

according to the multi-group differential volcano plots, the SI group exhibited significantly reduced L-glutamic acid levels compared to the SC group in both areas A and B (Figure 6C). The variable importance in projection results (Figure 6D and E) corroborated the L-glutamic acid trends observed across the groups, as shown in Figure 6C. Compared with the SC group, the SI group showed a notable increase in glutamine

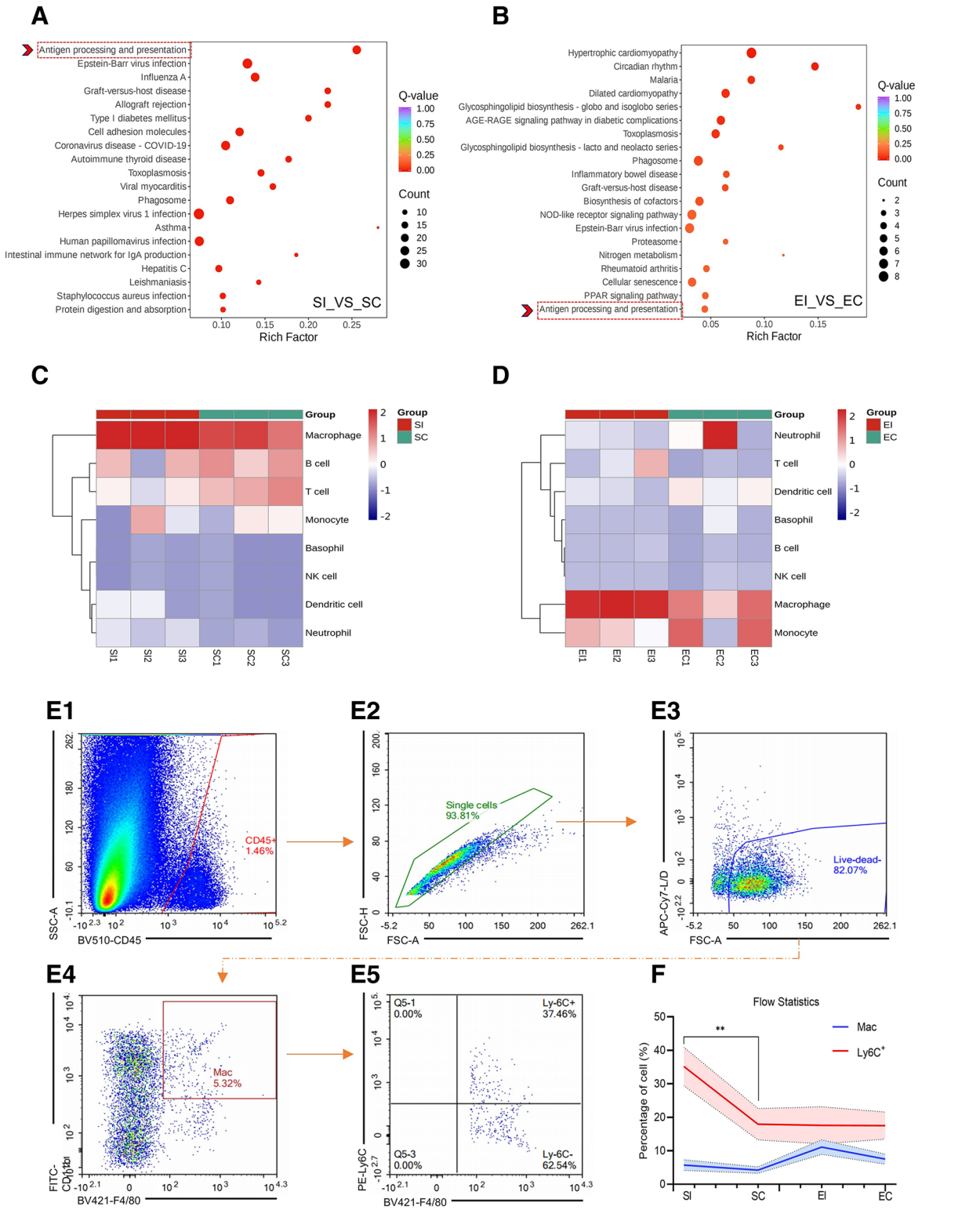

Figure 5. Changes in renal Ly6C⁺ macrophage contents. (A and B) Kyoto Encyclopedia of Genes and Genomes enrichment scatter plots from renal transcriptomes for SI_VS_SC and EI_VS_EC groups. (C and D) Analysis of immune cell infiltration in the kidneys. (E1–E5) Gating strategy for Ly6C⁺ macrophages in flow cytometry. (F) Flow cytometry statistical results (**$P < 0.01$). EC: Enduring control; EI: Enduring inflammation; SC: Single control; SI: Single inflammation.

(m/z = 147.0764), a direct antioxidant closely associated with L-glutamic acid. Further analysis of the spatial distributions of L-glutamic acid and glutamine (Figure 6F–I) revealed that in the single-dose pneumonia mouse model, L-glutamic acid levels decreased and glutamine levels increased in regions A and B of the kidneys, compared to those in normal mice. In contrast, the multiple-dose group had higher L-glutamic acid levels and lower glutamine levels in kidney regions A and B than the normal group.

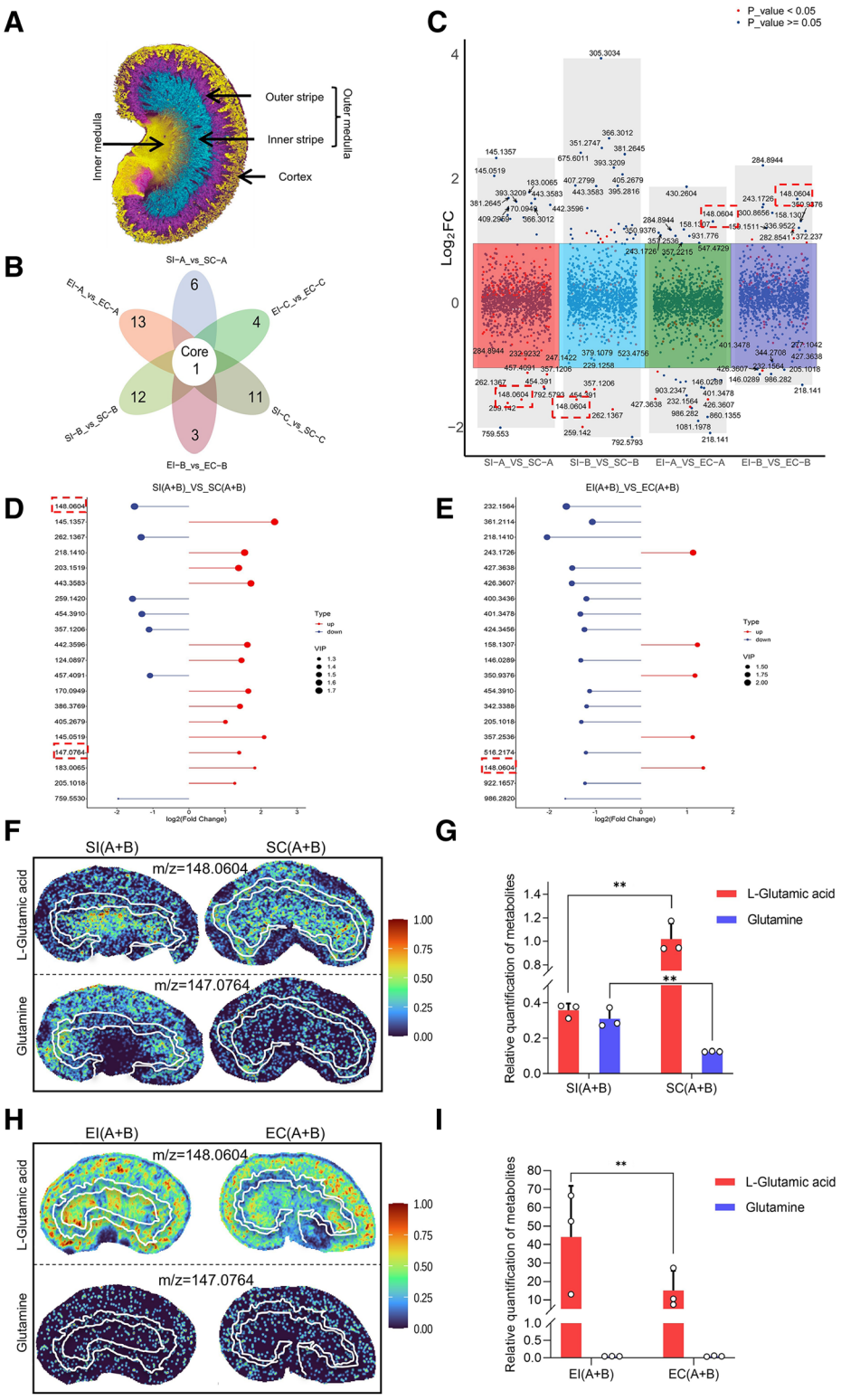

Figure 6. Transcriptomic study of differences in AAI-induced kidney damage in C57BL/6 mice. (A) Diagram illustrating the kidney spatial structure. (B) Venn diagram of differential metabolites. (C) Multi-group differential volcano plot for metabolites. (D and E) VIP lollipop charts. (F and G) Spatial distribution and statistical analysis of L-glutamic acid and glutamine in the SI_VS_SC group. (H and I) Spatial distribution and statistical analysis of L-glutamic acid and glutamine in the SI_VS_SC group, with significant findings (**$P < 0.01$). EC: Enduring control; EI: Enduring inflammation; SC: Single control; SI: Single inflammation; VIP: Variable importance in projection.

Ly6C+ macrophages alleviate oxidative stress in mRTECs by regulating the ITGA5/pAkt/pNrf2/NQO1 pathway through glutamine metabolism

To further investigate the interaction between Ly6C+ macrophages and renal tubular epithelial cells, we designed a co-culture experiment (Figure 7A). In this experiment, 10 mM L-glutamic acid was added to the upper chamber of a Transwell system, and 100 μM AAI was added to the lower chamber. After 24 h, we measured the L-glutamic acid and glutamine concentrations

in the supernatant from the lower chamber (the layer containing mRTECs) (Figure 7B). The supernatant from the lower chamber co-cultured with Ly6C$^+$ macrophages exhibited significantly increased levels of glutamine ($n = 3$; $P < 0.01$) and significantly decreased levels of L-glutamic acid compared with the control group ($n = 3$; $P < 0.01$). In the supernatant co-cultured with Ly6C$^-$ macrophages, although L-glutamic acid levels were significantly reduced compared to those in the control ($n = 3$; $P < 0.01$), Glutamine levels were similar to those in the control group. In addition, ROS levels in the mRTECs in the lower chamber were significantly lower in the Co-Ly6C$^+$ group than in the other groups (Figure 7C). These results were confirmed by fluorescence intensity measurements using a fluorometer (Figure 7D). Western blot analysis was performed to detect changes in ITGA5/pAkt/pNrf2/NQO1 protein levels (Figure 7E). Densitometric analysis revealed no significant differences in the primary bands of Nrf2 and Akt among the groups examined (Figure 7F). As shown in Figure 7G and H, the Co-Ly6C$^+$ group exhibited significantly lower levels of ITGA5, pNrf2, pAkt, and NQO1 than the control group ($n = 3$; $P < 0.01$). Conversely, the Co-Ly6C$^-$ group showed no significant difference in the expression of ITGA5, pNrf2, pAkt, or NQO1 proteins compared to the control group.

Discussion

Key findings

In China, the safety of herbal medicines that contain aristolochic acid remains a notable concern. The 2020 edition of the Chinese Pharmacopoeia includes only one herb, Xi Xin, and specifies that the AAI content must not exceed 0.001%[21]. However, given the frequent use of Xi Xin in decoctions and the broad market for these formulations, safety concerns surrounding aristolochic acid are highly sensitive and have substantial implications for public health and the development of traditional Chinese medicine. The risks associated with the clinical use of Xi Xin, particularly the formation of DNA adducts at commonly used doses, remain critical, that warrant resolution[22–23].

In our previously published preprint[24], we found that AAI present in clinical doses of Asarum did not lead to the formation of DNA adducts in mouse kidneys. Similarly, even when mice were administered an oral dose of AAI equivalent to more than 900 times that found in Asarum, as in the case of Aristolochia manshuriensis, no detectable levels of dA-ALI were observed in the renal tissue. These findings suggest that the short-term use of Asarum at clinical doses is relatively safe. Furthermore, in the current study, upon increasing the dose by 2,000 times, dA-ALI was detectable 24 h after administration. Next, we compared the responses of normal and pneumonia-state mice to AAI-induced renal damage and found that renal damage in C57 mice was significantly reduced under pneumonia conditions, indicating that pneumatic conditions have been shown to mitigate AAI-induced nephrotoxicity, further supporting the notion that the short-term use of Asarum within its indicated scope (respiratory disease) is relatively safe.

Mechanistically, the integration of spatial metabolomics and transcriptomics suggests that the observed phenomena may be related to the inherent mechanisms of the body that regulate oxidative stress. LPS-induced pneumonia stimulates antioxidant defenses in the kidneys and maintains a relatively low level of oxidative stress after AAI intake, thereby inhibiting the ITGA5/pAkt/pNrf2/NQO1 pathway. However, after multiple administrations of LPS, the kidney's tolerance threshold for oxidative stress was exceeded, elevating oxidative stress levels upon AAI intake, and activating the ITGA5/pAkt/pNrf2/NQO1 pathway. Spatial metabolomics results further revealed that an increased population of Ly6C$^+$ macrophages in the kidneys of the single-dose group used L-glutamic acid to produce the antioxidant glutamine, thereby reducing renal oxidative stress. This process was further verified through co-culture experiments. Glutamine has been shown to mitigate apoptosis in tubular cells[25] and alleviate renal dysfunction[26], supporting the hypothesis that glutamine has anti-inflammatory and cytoprotective properties in an AAI-induced renal damage model. Furthermore, Nrf2 contains numerous serine, threonine, and tyrosine residues that may serve as phosphorylation sites for various kinases[27]. Numerous pathways have been explored, including the mitogen-activated protein kinase cascade, PI3K-Akt pathway, protein kinase C, GSK3b pathway, and ERK signaling pathways. In addition, phosphorylation of Nrf2 may disrupt its interaction with Keap1, thereby facilitating the nuclear translocation of pNrf2[28]. According to a study published in the internationally renowned journal *Cancer Cell*, sustained activation of the PI3K-Akt signaling pathway leads to increased nuclear accumulation of pNrf2[29]. Our research also confirmed that elevated pAkt expression activates the pNrf2/NQO1 pathway.

Interpretations and implications

Research on macrophages has primarily focused on identifying phenotypes of macrophage subpopulations that regulate tissue damage and repair[30]. Typically, macrophages are classified into two types: M1, which are pro-inflammatory, and M2, which are anti-inflammatory[31–32]. However, conventional classification methods, based on a single *in vitro* stimulus, overlook the complexity of the renal microenvironment. A functional overlap exists between M1 and M2 macrophages[33–34], and analyses of the expression profiles of macrophages isolated from the liver post-injury have revealed that macrophages cannot be strictly categorized as either M1 or M2 at any given time point[35]. Therefore, in the current study, renal macrophages were classified into Ly6C$^+$ and Ly6C$^-$ subtypes based on Ly6C expression[36], which more accurately reflects the phenotypic changes in renal macrophages following AAI administration in mice exhibiting pneumonia or normal conditions. Glutamine can reportedly prevent acute kidney injury by modulating oxidative stress and apoptosis in renal tubular epithelial cells[37], whereas our study further demonstrated that renal Ly6C$^+$ macrophages use L-glutamic acid to produce glutamine, thereby participating in the regulation of oxidative stress.

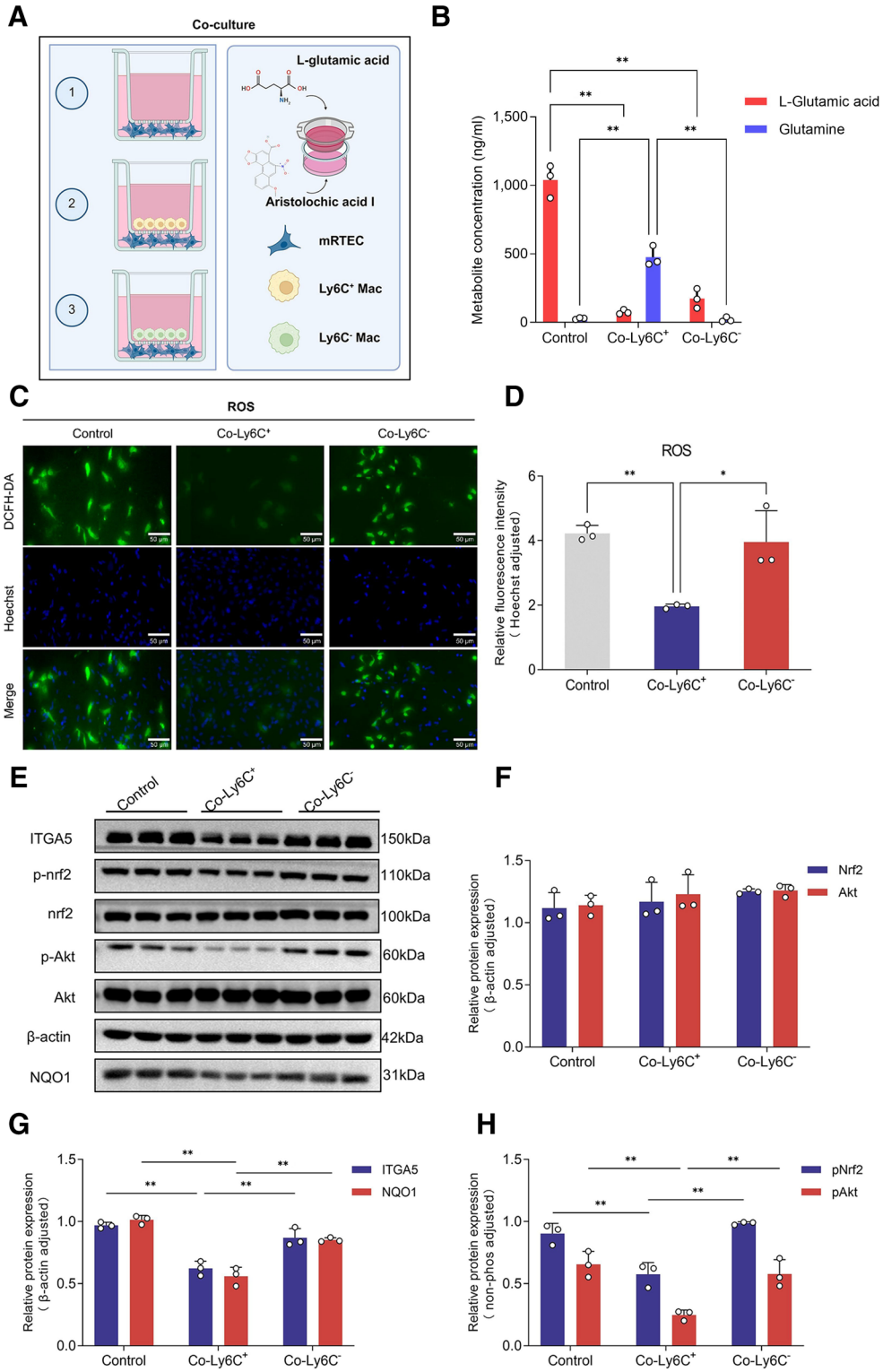

Figure 7. Co-culture experiment of Ly6C± macrophages with renal tubular epithelial cells. (A) Transwell co-culture system. (B) Levels of L-glutamic acid and glutamine in the supernatant from the lower chamber cells. (C) DCFH-DA probe detection of ROS levels in mRTECs. (D) Quantitative analysis of ROS fluorescence intensity in mRTECs using a multifunctional microplate reader. (E–H) Western blot and densitometric analyses of the ITGA5/pAkt/p-Nrf2 pathway. (*P < 0.05, **P < 0.01). DCFH-DA: 2′,7′-Dichlorodihydrofluorescein diacetate; mRTECs: Mouse renal tubular epithelial cells; ROS: Reactive oxygen species.

Notably, glutamine produced by macrophages is transported into renal parenchymal cells through solute carrier family transporter proteins, where it functions as an antioxidant[38]. Although macrophages exhibit substantial resistance to ROS[39–40], they are not completely immune to ROS-induced cell death. The protective effect of glutamine was observed within 72 h of inducing renal ischemia-reperfusion injury[37]. However, upon exposure to sustained oxidative stress over a prolonged period, macrophages accumulate

considerable amounts of oxidized proteins and lipids, leading to metabolic dysfunction. This accumulation leads to the loss of DNA integrity and inevitable cell death[41–42]. This finding effectively explains why the multiple-dose group in our experiment did not develop renal tolerance to AAI toxicity as observed in the single-dose group.

Future directions

This study raised several unresolved questions. ITGA5, a transmembrane signaling protein and member of the integrin family, links the extracellular matrix to the intracellular cytoskeleton and plays a role in various biological processes, including extracellular signal transduction, cell adhesion, and cell migration[43–44]. ITGA5 primarily functions by transducing extracellular signals, such as changes in ROS levels, as observed in the current study, and by regulating the interactions between the extracellular matrix and cells, rather than by directly participating in intracellular metabolic processes.

However, the mechanism by which ITGA5 influences Akt phosphorylation warrants further investigation. Additionally, fundamental differences exist between mouse and human macrophages in terms of LPS-induced metabolic reprogramming and reactive nitrogen species synthesis[45–46], and caution must be exercised when translating findings from mouse models to human data. Further research is needed to investigate the progression of kidney damage following short-term high-dose AAI exposure cessation and the effects of long-term low-dose AAI intake.

Conclusions

Our study confirmed that Xi Xin is relatively safe at clinical doses for short-term use, and its potential risks can be further reduced when used to treat pneumonia in a targeted manner. The kidneys of mice with pneumonia appear tolerant to AAI-induced toxicity and carcinogenicity. Using integrated spatial metabolomics and renal transcriptomic analyses, we found that this phenomenon may be associated with a mechanism regulating Glutamine-mediated oxidative stress defense. Moreover, $Ly6C^+$ macrophages use glutamine derived from L-glutamic acid as part of the regulatory process. These findings highlight the metabolic crosstalk between $Ly6C^+$ macrophages and renal tubular epithelial cells, wherein glutamine derived from $Ly6C^+$ macrophages potentially imparts antioxidative defense capabilities to the kidneys.

Conflict of interest statement

The authors declare no conflict of interest.

Funding

This study was supported by the Consulting Project Funds of the Chinese Academy of Engineering (2023-XZ-88, China), Key Program of the National Natural Science Foundation of China (81721002 and 82230118, China), and Key Program of the National Natural Science Foundation of China Regional Union Fund (U23A20519, China).

Author contributions

Chengxian Li contributed to investigation, writing—original draft; Yinkang Wang contributed to data curation, visualization; Shuanglin Qin contributed to methodology, project administration; Xiaoyan Zhan contributed to writing—review & editing; Xu Zhao contributed to writing—review & editing; Mingxia Fang contributed to writing—review & editing; Jiaying Li contributed to validation; Ming Niu contributed to methodology, supervision; Zhaofang Bai contributed to conceptualization, funding acquisition; and Xiaohe Xiao contributed to conceptualization; project administration; funding acquisition. The manuscript has been read and approved by all authors, meets the journal's criteria for authorship, and each author believes that the manuscript represents their honest work.

Ethical approval of studies and informed consent

All animal experiments were performed in accordance with the Guidelines for the Care and Use of Laboratory Animals and were approved by the Fifth Medical Centre of the PLA General Hospital, Beijing, China (ethical approval no. IACUC-2021-0010).

Acknowledgments

None.

Data availability

All data generated or analyzed during this study are included in this published article.

References

[1] Hu YS, Zhang JQ, Wei WL, et al. Comprehensive HRMS screening and risk assessments of aristolochic acid analogues in Asari Radix et rhizoma and related commercial health products. *J Agric Food Chem* 2024;72(13):7438–7456.
[2] Nie L, Wang X, Li J, et al. Content analysis and risk assessment of aristolochic acids in Chinese medicinal materials (decoction pieces). *Chin J Pharmacovigil* 2023;20:553–559.
[3] Kato R. Drug metabolism under pathological and abnormal physiological states in animals and man. *Xenobiotica* 1977;7(1-2):25–92.
[4] He ZX, Chen XW, Zhou ZW, et al. Impact of physiological, pathological and environmental factors on the expression and activity of human cytochrome P450 2D6 and implications in precision medicine. *Drug Metab Rev* 2015;47(4):470–519.
[5] Guo W, Shi Z, Zeng T, et al. Metabolic study of aristolochic acid I-exposed mice liver by atmospheric pressure matrix-assisted laser desorption/ionization mass spectrometry imaging and machine learning. *Talanta* 2022;241:123261.
[6] Chen J, Li H, Bai Y, et al. Spatially resolved multi-omics unravels region-specific responses, microenvironment remodeling and metabolic reprogramming in aristolochic acid nephropathy. *Innov Med* 2024;2:100066.
[7] Wang Z, He B, Liu Y, et al. In situ metabolomics in nephrotoxicity of aristolochic acids based on air flow-assisted desorption electrospray ionization mass spectrometry imaging. *Acta Pharm Sin B* 2020;10(6):1083–1093.
[8] Wang X, Song J, Dong Y, et al. Qualitative and quantitative bioanalytical methods validation of aristolochic acid DNA adducts and application in human formalin-fixed paraffin-embedded hepatocellular carcinoma tissues. *bioRxiv*.
[9] Chen S, Dong Y, Qi X, et al. Aristolochic acids exposure was not the main cause of liver tumorigenesis in adulthood. *Acta Pharm Sin B* 2267;12(2):2252–2267.
[10] Li CX, Xiao XH, Li XY, et al. Stir-fried semen armeniacae amarum suppresses aristolochic acid I-induced nephrotoxicity and DNA adducts. *Chin J Integr Med* 2025;31(2):142–152.

[11] Alexandrov T. Spatial metabolomics and imaging mass spectrometry in the age of artificial intelligence. *Annu Rev Biomed Data Sci* 2020;3:61–87.
[12] Bemis KD, Harry A, Eberlin LS, et al. Probabilistic segmentation of mass spectrometry (MS) images helps select important ions and characterize confidence in the resulting segments. *Mol Cell Proteomics* 2016;15(5):1761–1772.
[13] Wen J, Qin S, Li Y, et al. Flavonoids derived from licorice suppress LPS-induced acute lung injury in mice by inhibiting the cGAS-STING signaling pathway. *Food Chem Toxicol* 2023;175:113732.
[14] Yao Q, Wen J, Chen S, et al. Shuangdan Jiedu decoction improved LPS-induced acute lung injury by regulating both cGAS-STING pathway and inflammasome. *J Ethnopharmacol* 2025;336:118661.
[15] Kinner A, Wu W, Staudt C, et al. Gamma-H2AX in recognition and signaling of DNA double-strand breaks in the context of chromatin. *Nucleic Acids Res* 2008;36(17):5678–5694.
[16] Qu M, Xu H, Chen J, et al. Differential comparison of genotoxic effects of aristolochic acid I and II in human cells by the mass spectroscopic quantification of γ-H2AX. *Toxicol In Vitro* 2022;81:105349.
[17] Li Y, Xu H, Cai D, et al. Integration of transcriptomic, proteomic and metabolomic data to reveal the biological mechanisms of AAI injury in renal epithelial cells. *Toxicol In Vitro* 2021;70:105054.
[18] Liu X, Wu J, Wang J, et al. Mitochondrial dysfunction is involved in aristolochic acid I-induced apoptosis in renal proximal tubular epithelial cells. *Hum Exp Toxicol* 2020;39(5):673–682.
[19] Chen Z, Ji C, Shen Q, et al. Tissue-specific deconvolution of immune cell composition by integrating bulk and single-cell transcriptomes. *Bioinformatics* 2020;36(3):819–827.
[20] Römpp A, Guenther S, Takats Z, et al. Mass spectrometry imaging with high resolution in mass and space (HR^2 MSI) for reliable investigation of drug compound distributions on the cellular level. *Anal Bioanal Chem* 2011;401(1):65–73.
[21] Fang ZE, Guo Y, Wang Z, et al. Asari radix et rhizoma consumption lacks relevance for hepatocellular carcinoma in patients: a retrospective cohort study. *Chin Herb Med* 2022;14(3):470–475.
[22] Zhao X, Bai ZF, Zhan XY, et al. Safety evaluation of traditional Chinese medicine: New era, new strategy. *Acupunct Herb Med* 2024;4(2):171–175.
[23] Li X, Chen RY, Duan SN, et al. Research progress on the toxicity of Asari Radix et Rhizoma. *Acupunct Herb Med* 2024;4(2):197–208.
[24] Wang YK, Li CX, Qin SL, et al. Pneumonia activates renal antioxidant defense function to reduce the damage of aristolochic acid I through Keap1/Nrf2/NQO1 signaling pathway. PREPRINT (Version 1) available at Research Square 2024.
[25] Kim YS, Jung MH, Choi MY, et al. Glutamine attenuates tubular cell apoptosis in acute kidney injury via inhibition of the c-Jun N-terminal kinase phosphorylation of 14-3-3. *Crit Care Med* 2009;37(6):2033–2044.
[26] Naserzadeh R, Jafaripour L, Eslamifar Z, et al. The effect of receiving L-glutamine on the reduction of renal tissue damages and renal function recovery following gentamicin-induced nephrotoxicity in rats. *J Babol Univ Med Sci* 2021;23:267–274.
[27] Rojo AI, Medina-Campos ON, Rada P, et al. Signaling pathways activated by the phytochemical nordihydroguaiaretic acid contribute to a Keap1-independent regulation of Nrf2 stability: role of glycogen synthase kinase-3. *Free Radic Biol Med* 2012;52(2):473–487.
[28] Huang HC, Nguyen T, Pickett CB. Phosphorylation of Nrf2 at Ser-40 by protein kinase C regulates antioxidant response element-mediated transcription. *J Biol Chem* 2002;277(45):42769–42774.
[29] Mitsuishi Y, Taguchi K, Kawatani Y, et al. Nrf2 redirects glucose and glutamine into anabolic pathways in metabolic reprogramming. *Cancer Cell* 2012;22(1):66–79.
[30] Wynn TA, Vannella KM. Macrophages in tissue repair, regeneration, and fibrosis. *Immunity* 2016;44(3):450–462.
[31] Locati M, Curtale G, Mantovani A. Diversity, mechanisms, and significance of macrophage plasticity. *Annu Rev Pathol* 2020;15:123–147.
[32] Huen SC, Cantley LG. Macrophage-mediated injury and repair after ischemic kidney injury. *Pediatr Nephrol* 2015;30(2):199–209.
[33] Lee S, Huen S, Nishio H, et al. Distinct macrophage phenotypes contribute to kidney injury and repair. *J Am Soc Nephrol* 2011;22(2):317–326.
[34] Dessing MC, Tammaro A, Pulskens WP, et al. The calcium-binding protein complex S100A8/A9 has a crucial role in controlling macrophage-mediated renal repair following ischemia/reperfusion. *Kidney Int* 2015;87(1):85–94.
[35] Ramachandran P, Pellicoro A, Vernon MA, et al. Differential Ly-6C expression identifies the recruited macrophage phenotype, which orchestrates the regression of murine liver fibrosis. *Proc Natl Acad Sci U S A* 2012;109(46):E3186–E3195.
[36] Yang Q, Wang Y, Pei G, et al. Bone marrow-derived Ly6C- macrophages promote ischemia-induced chronic kidney disease. *Cell Death Dis* 2019;10(4):291.
[37] Thomas K, Zondler L, Ludwig N, et al. Glutamine prevents acute kidney injury by modulating oxidative stress and apoptosis in tubular epithelial cells. *JCI Insight* 2022;7(21):e163161.
[38] Cheng X, Wang Y, Gong G, et al. Design strategies and recent development of bioactive modulators for glutamine transporters. *Drug Discov Today* 2024;29(2):103880.
[39] Miyazaki T, Kanatsu-Shinohara M, Ogonuki N, et al. Glutamine protects mouse spermatogonial stem cells against NOX1-derived ROS for sustaining self-renewal division in vitro. *Development* 2023;150(20):dev201157.
[40] Xiao Z, Deng S, Liu H, et al. Glutamine deprivation induces ferroptosis in pancreatic cancer cells. *Acta Biochim Biophys Sin (Shanghai)* 2023;55(8):1288–1300.
[41] Wang B, Wang Y, Zhang J, et al. ROS-induced lipid peroxidation modulates cell death outcome: mechanisms behind apoptosis, autophagy, and ferroptosis. *Arch Toxicol* 2023;97(6):1439–1451.
[42] Chen A, Huang H, Fang S, et al. ROS: A "booster" for chronic inflammation and tumor metastasis. *Biochim Biophys Acta Rev Cancer* 2024;1879(6):189175.
[43] Li D, Sun A, Zhang L, et al. Elevated ITGA5 facilitates hyperactivated mTORC1-mediated progression of laryngeal squamous cell carcinoma via upregulation of EFNB2. *Theranostics* 2022;12(17):7431–7449.
[44] Zhang C, Yu Z, Yang S, et al. ZNF460-mediated circRPPH1 promotes TNBC progression through ITGA5-induced FAK/PI3K/AKT activation in a ceRNA manner. *Mol Cancer* 2024;23(1):33.
[45] Sabogal-Guáqueta AM, Marmolejo-Garza A, Trombetta-Lima M, et al. Species-specific metabolic reprogramming in human and mouse microglia during inflammatory pathway induction. *Nat Commun* 2023;14(1):6454.
[46] Vijayan V, Pradhan P, Braud L, et al. Human and murine macrophages exhibit differential metabolic responses to lipopolysaccharide—a divergent role for glycolysis. *Redox Biol* 2019;22:101147.